Journal of Power Sources 192 (2009) 618–626

Contents lists available at ScienceDirect

Journal of Power Sources

journal homepage: www.elsevier.com/locate/jpowsour

Influence of S and Ni co-doping on structure, band gap and electrochemical properties of lithium manganese oxide synthesized by soft chemical method

M.W. Raja, S. Mahanty, R.N. Basu*

Fuel Cell and Battery Division, Central Glass and Ceramic Research Institute, CSIR, Kolkata 700032, India

ARTICLE INFO

Article history:
Received 12 January 2009
Received in revised form 24 February 2009
Accepted 8 March 2009
Available online 27 March 2009

Keywords:
Lithium-ion battery
$LiMn_2O_4$
Self-combustion reaction
Electrochemical properties

ABSTRACT

Ni-doped lithium manganese oxysulfides with a nominal composition of $LiNi_xMn_{2-x}O_{4-\delta}S_\delta$ ($0 \le x \le 0.5$ and $0 \le \delta \le 0.1$) have been synthesized by an alanine-assisted, low-temperature combustion process, followed by calcination at 700 °C in air. Quantitative X-ray phase analyses show that the spinel structure of $LiMn_2O_4$ is retained for all compositions. However, analysis of the vibrational peaks observed in Fourier transformed infrared (FTIR) spectroscopy suggests that the Fd3m crystal symmetry is retained only up to $x \le 0.4$ and changes to $P4_332$ symmetry for $x = 0.5$. A systematic change in microstructure is observed with increasing Ni content in presence of S. The shape of the particles changes from spherical ($LiMn_2O_4$) to icosahedron ($LiNi_{0.2}Mn_{1.8}O_{4-\delta}S_\delta$) to octahedron ($LiNi_{0.5}Mn_{1.5}O_{4-\delta}S_\delta$). UV–vis spectroscopy shows that the band structure of pristine $LiMn_2O_4$ is strongly influenced by hybridization among Mn 3d and O 2p orbitals near the Fermi level and the band gap (1.45 eV) gradually decreases with increasing nickel content and reaches the minimum (1.35 eV) for $LiNi_{0.4}Mn_{1.6}O_{4-\delta}S_\delta$. Electrochemical results on 2032 coin-type cells, fabricated with the synthesized powders as the positive electrode (cathode) and Li metal as the negative electrode (anode), reveal that the substitution of S for O and Ni for Mn in $LiMn_2O_4$ enhances the structural integrity of the spinel host, which in turn increases the electrochemical cycleability. A high initial discharge capacity of 155 mAh g^{-1} is obtained for a $LiNi_{0.4}Mn_{1.6}O_{4-\delta}S_\delta$/Li cell with about 87% capacity retention (135 mAh g^{-1}) after 25 cycles at a current density of 0.2 mA cm^{-2}. All $LiNi_xMn_{2-x}O_{4-\delta}S_\delta$/Li cells ($x = 0.2$–$0.5$) show excellent reversibility with nominal capacity fading (0.04–0.2 mAh per cycle) at a current density of 0.2 mA cm^{-2}.

1. Introduction

$LiMn_2O_4$ has many favourable features as a positive electrode (cathode) material in lithium-ion batteries, e.g., high voltage, high specific energy, low cost and environmental benignity [1–4]. On the other hand, it shows poor cycling behaviour caused by a fast capacity fading in the 3 V range because of the Jahn–Teller distortion of the [MnO_6] octahedron, as well as in the 4 V range because of manganese dissolution during lithium-ion intercalation/deintercalation [5]. Partial substitution of manganese by various metal elements to form $LiM_xMn_{2-x}O_4$ (M = Co, Mg, Cr, Ni, Fe, Al, Ti and Zn) has been attempted to overcome these problems [6–9]. Some favourable results have been obtained, namely, a reduction of manganese dissolution [10], enhancement of Li ion extraction [11], single-phase charge/discharge behaviour [12], stronger structural reinforcement of $LiMn_{2-x}M_xO_4$ [13], and reduction of the Jahn–Teller effect [14].

In general, with a small amount of substitution in the Mn site, the dopant slightly reduces the initial capacity at the 4 V plateau, but markedly improves the cycle-life. An extensive amount of doping results in a significant decrease in capacity at the 4 V plateau, but a higher voltage plateau appears in the 5 V region (4.5–5.0 V) depending upon the redox coupling [15]. In this respect, Ni substitution in $LiMn_2O_4$ is very promising due to its high discharge capacity and a dominant high voltage plateau at around 4.7 V. On the other hand, synthesis of heavily Ni-doped $LiMn_2O_4$, i.e., $LiMn_{1.5}Ni_{0.5}O_4$, often results in a small amount of NiO impurity due to oxygen deficiency in the spinel lattice, along with the possible presence of a small quantity of Mn^{3+} in the matrix, that results in lower capacity and poor cycling stability. To overcome this problem and to increase the structural and cycling stability of $LiNi_{0.5}Mn_{1.5}O_4$ in the 5 V region, anionic substitution (F, S) in the oxygen sublattice has been investigated [16–23]. Molenda et al. [17] and Park et al. [20] have shown that a small amount of isoelectronic sulfur in $LiMn_2O_4$ might be helpful to circumvent the Jahn–Teller effect. In the present work, $LiMn_2O_4$ has been co-doped by Ni and S to find an optimum composition for $LiNi_xMn_{2-x}O_{4-\delta}S_\delta$ ($0 \le x \le 0.5$ and $0 \le \delta \le 0.1$). A study is undertaken of the effect of co-doping on physical properties such as structure,

* Corresponding author. Fax: +91 33 2473 0957.
E-mail address: rnbasu@cgcri.res.in (R.N. Basu).

0378-7753/$ – see front matter © 2009 Elsevier B.V. All rights reserved.
doi:10.1016/j.jpowsour.2009.03.040

microstructure, optical band gap, and the electrochemical performance.

2. Experimental

Nickel-doped lithium manganese oxysulfide powders ($LiNi_xMn_{2-x}O_{4-\delta}S_\delta$, where $0 \le x \le 0.5$ and $0 \le \delta \le 0.1$) were synthesized by a single-step combustion process. $LiNO_3$ (SRL, 99.5%), $Mn(Ac)_2{,}4H_2O$ (Merck, 99.5%), $Ni(NO_3)_2$ (SRL, 99%), Li_2S (Alfa Aeser, 99%) and L-alanine (Merck, 99.5%) were used as the starting materials. First, an aqueous solution of manganese acetate, nickel nitrate, lithium sulfide and lithium nitrate (in stoichiometric ratio) was prepared and stirred on a hot plate at about 150 °C. Then, a saturated aqueous solution of L-alanine was added so that the alanine:nitrate ratio remained at 1:1. Dilute nitric acid (70 vol.%) was added drop-wise to the solution to compensate the acetates. On vigorous stirring and heating, the whole solution turned into a viscous gel. Thereafter, instantaneous combustion occurred to produce a blackish ash. The detailed synthesis procedure is shown schematically in Fig. 1. The synthesized samples in this investigation are designated as LMN2S ($LiNi_{0.2}Mn_{1.8}O_{4-\delta}S_\delta$), LMN3S ($LiNi_{0.3}Mn_{1.7}O_{4-\delta}S_\delta$), LMN4S ($LiNi_{0.4}Mn_{1.6}O_{4-\delta}S_\delta$) and LMN5S ($LiNi_{0.5}Mn_{1.5}O_{4-\delta}S_\delta$). For comparison, pristine $LiMn_2O_4$ and $LiMn_{1.5}Ni_{0.5}O_4$ compounds were also synthesized by the method described above and is referred to as LM and LMN5. The code name of the samples along with the corresponding compositions is listed in Table 1.

X-ray diffractograms were recorded on a Philips X'pert X-ray diffractometer with Cu Kα radiation at 40 kV and 40 mA. The X-ray data were collected in the 2θ range 10–70° at a scan rate of 1° per min and a dwell time of 0.02 s. Rietveld refinement of the

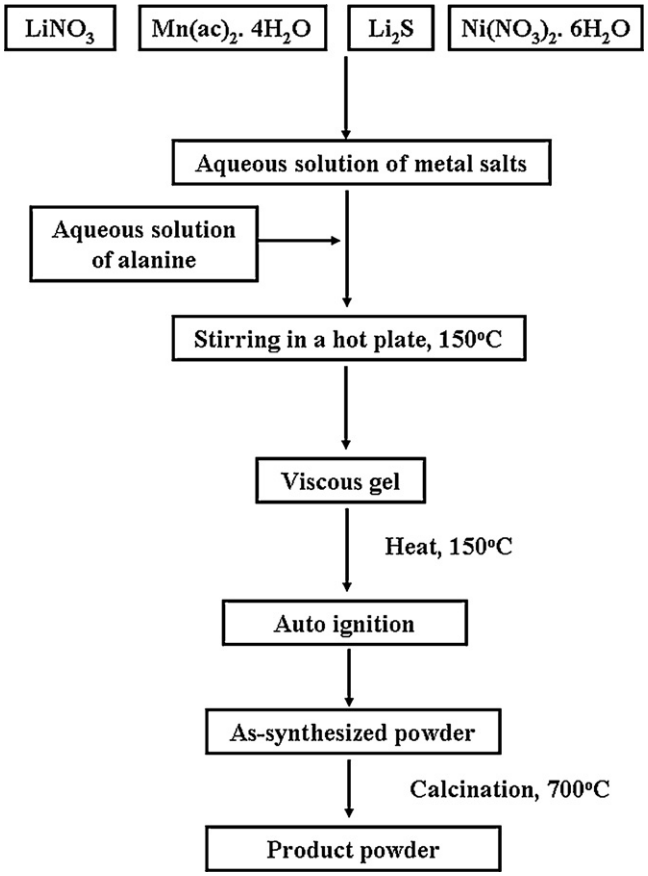

Fig. 1. Schematic of powder synthesis process.

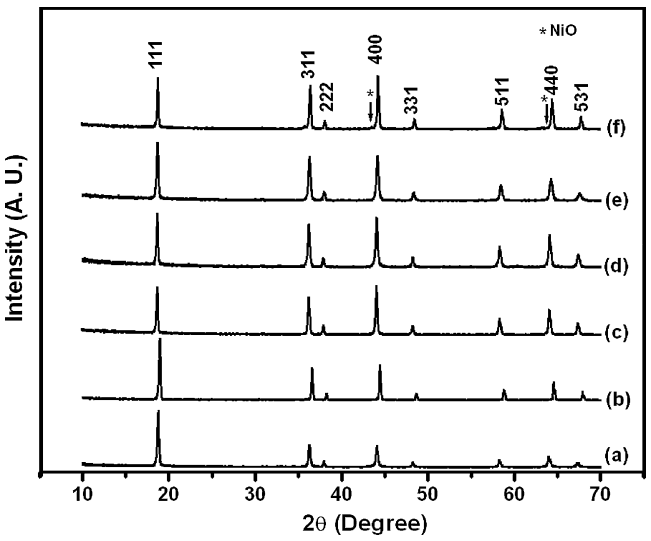

Fig. 2. X-ray diffractograms of (a) LM, (b) LMN5, (c) LMN2S, (d) LMN3S, (e) LMN4S, and (f) LMN5S powders calcined at 700 °C.

powder diffraction profiles and quantitative phase analysis were performed using a pseudovoight function by PANalytical Highscore Plus software. Size–strain analysis was conducted by comparing the profile width of a standard silicon scan to account for instrument broadening. Fourier transform infrared (FTIR) spectroscopy was performed with a BOMEN infrared spectrophotometer to determine the structure co-ordination of the synthesized powders. For FTIR, each sample was mixed with KBr and examined in the wave number range 4000–400 cm^{-1}. UV–vis absorption spectra were recorded by a Shimadzu (UV3100) spectrophotometer in the wavelength range 2000–200 nm to obtain information about the optical transitions. The microstructure and the morphology of the powders were studied by field emission scanning electron microscopy (FESEM) with a Zeiss microscope (Gemini Supra 35). Energy dispersive X-ray analysis (EDX) and elemental mapping were also carried out using the same instrument. Two-probe, room-temperature, electrical conductivity measurements were conducted with a Solartron 1260 impedance analyzer on sintered (800 °C) pellets of the oxysulfide powders.

For electrochemical testing, 2032 coin-type cells were fabricated. A slurry was prepared by mixing the active material (80 wt.%) with acetylene black (8 wt.%) and binder (12 wt.% polyvinylidene fluoride, PVDF, dissolved in n-methyl-2-pyrrolidone, NMP). The mixed slurry was coated on an aluminum foil of 20 μm thickness. The coated films were then dried at 120 °C for 12 h, pressed, and then punched into a circular disc (diameter ~16 mm) that was used as a cathode. The weight of a typical cathode was 0.03 g (including Al-foil) with an active material of 0.02 g. The electrode thicknesses were in the range of 80–110 μm (excluding Al-foil). 2032 coin cells were assembled in a glove box (MBRAUN, Germany), in which both oxygen and moisture levels were kept below 1.0 ppm. A complete cell comprised a cathode, celgard 2300 as the separator, and lithium metal foil as the anode. 1 M $LiPF_6$ dissolved in a mixture of ethylene carbonate (EC) and dimethyl carbonate (DMC) (1:1 by volume ratio) was used as the electrolyte. Galvanostatic charge–discharge cycles between 3.4 and 5 V were carried out with an automated battery tester (BT 2000, Arbin, USA).

3. Results and discussion

X-ray diffractograms of LM, LMN5, LMN2S, LMN3S, LMN4S and LMN5S powders calcined at 700 °C are shown in Fig. 2. For all samples, the diffraction peaks can be indexed to a spinel structure with

Table 1
Vibrational peaks obtained from various Ni-doped oxysulfide compounds.

Code name	Compounds	Peaks in spectral range 400–600 cm^{-1}	Reference
LM	$LiMn_2O_4$	511, 615	[30]
LMN5	$LiNi_{0.5}Mn_{1.5}O_4$	470, 607	Present work
LMN2S	$LiNi_{0.2}Mn_{1.8}O_{4-\delta}S_\delta$	511, 621	
LMN3S	$LiNi_{0.3}Mn_{1.7}O_{4-\delta}S_\delta$	509, 605	
LMN4S	$LiNi_{0.4}Mn_{1.6}O_{4-\delta}S_\delta$	512, 610	
LMN5S	$LiNi_{0.5}Mn_{1.5}O_{4-\delta}S_\delta$	463, 496, 560, 593,630	
–	$LiNi_{0.5}Mn_{1.5}O_4$, calcined at 600 °C for 24 h	432, 469, 479, 505, 556, 589, 622, 647	[32]

Fd3m symmetry. Previous studies have shown [24,25] that synthesis of single-phase $LiNi_{0.5}Mn_{1.5}O_4$ often results in accompanying undesired impurities, such as NiO and Li_xNi_yO, in the final product, that deteriorate the electrochemical behaviour. In the present study, no additional peak is found for the LMN5 sample with the maximum Ni content. In the case of the LMN5S sample, however, there are a few weak reflections of NiO that might arise from oxygen deficiency in the structure. The high intensity and sharpness of the (4 0 0) peak indicate that highly crystallized powders have been synthesized [26]. It is particularly interesting that the relative intensity ratio of the (4 0 0/1 1 1) peaks of the oxysulfides is higher than that of the pristine sample, which reflects better crystallinity.

To observe the effect of Ni and S co-doping on the unit cell properties, the lattice parameters were calculated and the variation of lattice parameter with the amount of nickel content is plotted in Fig. 3. Pristine $LiMn_2O_4$ shows a lattice parameter value of $a = 8.230$ Å. A gradual linear decrease in 'a' has been observed with increasing Ni content for all the compositions studied. These results suggest that in the presence of S, substitution of Mn by Ni takes place for all compositions up to Ni = 0.5, although it is not possible to estimate the amount of sulfur quantitatively for different Ni compositions. A close examination of the (4 0 0) peak (as shown in the inset of Fig. 3) reveals an interesting shift in peak position. For the pristine $LiMn_2O_4$ (LM), the (4 0 0) peak appears at $2\theta = 44.06$. When only Ni is introduced (LMN5), the peak shifts to the right to $2\theta = 44.44$. When Ni is co-doped with S (sample LMN2S), the peak further shifts back to the left ($2\theta = 44.08$) to nearly the original 2θ value and thereby indicates substitution of O by S. Thus, the observed decrease in the lattice constant with an increasing amount of nickel may probably be attributed to an increase in the concentration of Mn^{4+} due to the oxidation of Mn^{3+} to Mn^{4+} caused by the catalytic activity of S, together with the simultaneous substitution of Mn^{3+} ions with nickel ions [27,28]. Such kind of change in the lattice parameter may reflect a change in the metal–oxygen bonding. The Ni–O bond is stronger than the Mn–O bond and therefore will give rise to a smaller lattice parameter [29]. Thus, a stronger metal–oxygen bonding can reinforce the [MO_6] octahedron in the spinel and may restrain the Jahn–Teller effect.

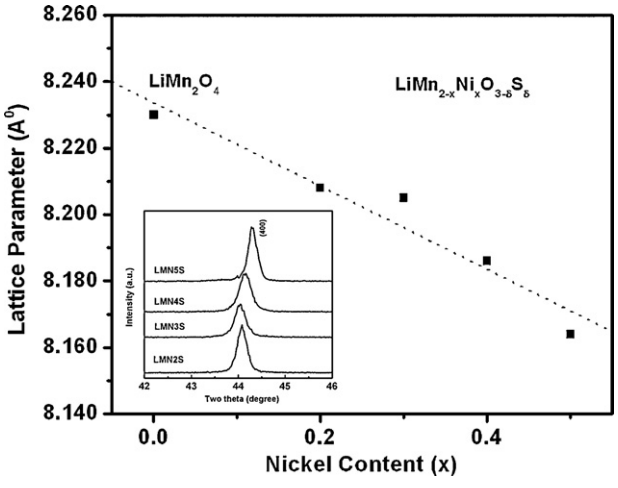

Fig. 3. Variation of lattice constant with nickel content in $LiNi_xMn_{2-x}O_{4-\delta}S_\delta$. Inset shows an enlarge portion ($2\theta = 42$–46°) taken from Fig. 2.

FTIR spectroscopy is considered to be an effective tool in solid-state chemistry because it provides information on the structural environment of inorganic solids. FTIR spectra of LMN2S, LMN3S, LMN4S and LMN5S samples in the wave number range of 400–4000 cm^{-1} are shown in Fig. 4. The bands observed in the range of 400–600 cm^{-1} are characteristic of metal–oxygen (M–O) vibration peaks and reflect the structural environment of MO_6 octahedra. In Fig. 4(a)–(c), two distinct peaks in the region of 509–621 cm^{-1} are observed for LMN2S, LMN3S and LMN4S that are attributed to the Ni–O and Mn–O vibrations originating from MO_6 octahedra. On the other hand, several peaks are observed in case of LMN5S at 463, 496, 560, 593 and 630 cm^{-1} [shown in the inset of Fig. 4(d)]. A comparison of peak positions of pure $LiMn_2O_4$ along with other Ni and S co-doped samples are given in Table 1. In our previous study [30], it was found that for pristine $LiMn_2O_4$ (LM) only two distinct characteristic peaks were observed at 511 and 615 cm^{-1} [30]. Only a slight shifting of these peak positions at 470 and 607 cm^{-1} is observed for the LMN5 sample (not shown here). However, Ni–O vibration peaks, due to the possible presence of a trace amount of NiO impurity, cannot be separated as these overlap with the strong Mn–O vibration peaks. It has been reported earlier [31,32] extensive annealing of heavily nickel doped $LiNi_{0.5}Mn_{1.5}O_4$ at 600 °C for 24 h results in structural transformation of Fd3m to an ordered $P4_332$ superstructure due to extensive Ni and Mn ordering in the crystal lattice [31,32]. This structural evolution could not, however be detected by XRD because of the similar atomic scattering factors of Ni and Mn. Fig. 4(a)–(c) shows that from the LMN2S to the LMN4S system no other peaks are found except two peaks characteristic of MO_6 vibrations. By contrast, a number of peaks at 463, 496, 560, 593 and 630 cm^{-1} are observed for LMN5S [Fig. 4(d)] and may result from lattice ordering of Ni and Mn in this Ni and S co-doped sample. For a better comparison, the peak positions of all these samples are listed in Table 1.

An FESEM micrograph of the as-synthesized powder of LMN2S prior to calcination is given in Fig. 5(a). It shows a uniform morphology with a particle size in the range of 80–100 nm. The particles are spherical and loosely bound to each other. This type of morphology is observed for all other as-synthesized powders, irrespective of the Ni or S content. Such agglomeration-free morphology in the as-synthesized powder helps to reduce the particle size distribution in the final product after calcination at high temperature (700 °C). Generally, agglomerated morphology results in a broad particle size distribution which may affect the electrochemical properties of the electroactive materials. It is mainly the fuel in combustion synthesis that determines the nature of the agglomeration. A previous study [30] showed that when alanine is used as the fuel in combustion, it evolves a considerable amount of heat and gaseous species near the flame temperature which helps in the formation of agglomeration-free, loosely bound particles [30]. FESEM micrographs of the calcined powders are shown in Fig. 5(b)–(f). An agglomerated morphology with loosely bound spherical particles is

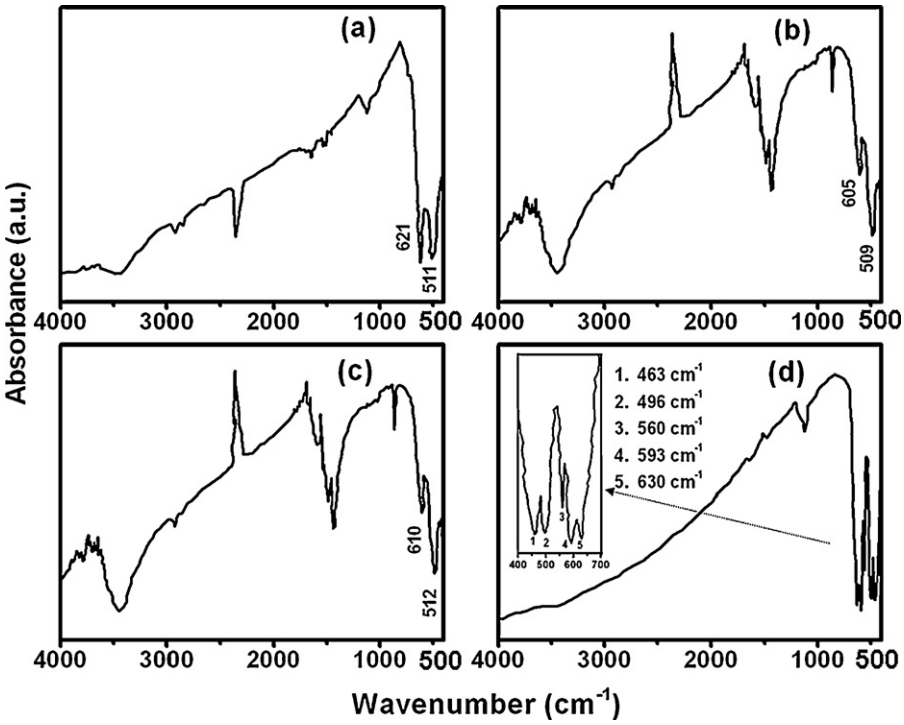

Fig. 4. FTIR spectra of (a) LMN2S, (b) LMN3S, (c) LMN4S, and (d) LMN5S.

observed in case of pristine $LiMn_2O_4$ (LM), Fig. 5(b). A similar type of morphology is seen in Fig. 5(b) for LMN5, which indicates that doping with Ni only does not significantly alter the morphology of the pristine compound. By contrast, a drastic change in morphology occurs in the Ni and S co-doped sample e.g., LMN2S as shown in Fig. 5(d). Polygonal-shaped grains having distinct faces could be clearly observed. Similar multifaceted morphology is also seen in case of LMN3S (not shown here) and LMN4S [Fig. 5(e)]. With further increase in nickel content to 0.5, i.e., for LMN5S, the polygonal shape changes to a clear octahedral shape [Fig. 5(f)]. Such microstructural evolution may be due to the catalytic activity of S in the octahedra of the spinel matrix. To confirm the presence of S within the grains, EDX analysis was conducted on a selective area of LMN4S [Fig. 6(a)] and the corresponding EDX profile is shown in Fig. 6(g). The presence of Mn, Ni, O and S is clearly observed in the EDX profile in addition to several other elements (Si, Ca, Cl, etc.) which come from the underlying glass substrate that was used to prepare the sample for EDX analysis. Lithium could not be detected as it is outside the EDX detection range. To confirm further whether S is present inside the grains or in the substrate, elemental mapping was performed on the same area for O, Si, S, Mn and Ni; the results are shown in Fig. 6(b)–(f), respectively. Whereas the signals for O, Mn and Ni come from the grains, the signal for Si comes from the substrate. Also, the majority of signals for S arise from grains that have a uniform distribution of S. For both pristine $LiMn_2O_4$ (LM) and $LiNi_{0.5}Mn_{1.5}O_4$ (LMN5) powder, the particle size is in the range of 60–150 nm. On the other hand, for the oxysulfides, the particle size increases by more than one order of magnitude to the range of 1–2 μm. This may be due to the catalytic activity of sulfur the during the synthesis process. The migration of sulfur into the bulk phase of oxysulfides may induce particle growth. Similar grain growth due to the presence of S has also been reported for different materials such as $Li_{1+x}NiO_{2-y}S_y$ [28], $Li_{1.03}Al_{0.2}Mn_{1.8}O_{3.96}S_{0.04}$ [33], ZrO_2 [34] and UO_2 [35], although no clear mechanism could be established. Goodenough [36] conducted a study on the electrochemical properties of thiospinel $Li_xTi_2S_2$, and proposed that the relatively larger size and polarizability of sulfur may reduce the structural strain when introduced in the spinel matrix and thereby produce a stable structure. On the other hand, Park et al. [28] examined the $Li_{1+x}NiO_{2-y}S_y$ system and suggested that the presence of sulfur helps the oxidation of metals and plays a crucial role in stabilizing the structure. Thus, although the mechanism of the catalytic activity of S is not fully understood, the microstructural features observed in the present study suggest that co-doping of nickel and sulfur in $LiMn_2O_4$ has a distinct effect on the microstructure, as well as on the particle size of the oxysulfides, which might also influence their structural stability and electrochemical performance.

UV–vis spectroscopy is a very useful technique for estimating the optical band gap of a ceramic semiconductor [30,37]. The optical band gap is very much related to the electronic conductivity of the materials. Fig. 7 shows the UV–vis absorption spectra, taken in the reflectance mode, for LM, LMN5, LMN2S, LMN3S, LMN4S and LMN5S powders. Derivative plots of the absorption spectra of all these samples are plotted and compared in Fig. 8. In a previous study [30], a band gap of 1.43 eV was found for the pristine $LiMn_2O_4$ compound. Here, it is found that the band gap is reduced to a value of 1.36 eV for 0.5 mol% Ni-doped $LiMn_2O_4$ (LMN5). It is well known that the band structure of $LiMn_2O_4$ or Ni-doped $LiMn_2O_4$ is strongly influenced by hybridization among transition metal 3d and O 2p orbitals, while Li remains in an ionic form. Thus, the decrease in band gap may be explained in terms of the total theoretical density of states (DOS) of pristine $LiMn_2O_4$ and $LiNi_{0.5}Mn_{1.5}O_4$ samples, as suggested by Liu et al. and Shi et al. (inset of Fig. 7) [38,39]. It can be seen that the shapes of the Mn 3d and O 2p bands do not alter significantly with Ni doping. That is, the Mn 3d bands are mostly distributed in the high-energy range near the Fermi level, while the O 2p bands are mainly dispersed in the low-energy range. It is noted, however, that some extra peaks appear in the case of $LiNi_{0.5}Mn_{1.5}O_4$ near the Fermi level compared with those for pristine $LiMn_2O_4$. Apparently, these new bands arise from the doping of Ni 3d. At the same time, additional new O 2p bands accompanying Ni 3d appear in nearly the same energy level due to interaction between Ni and O. Therefore, the gap between the Mn 3d and O 2p band decreases gradually and the corresponding band gap is low-

ered. In case of nickel oxysulfide compounds, the band gap values of LMN2S, LMN3S, LMN4S and LMN5S are 1.45, 1.41, 1.35 and 1.39 eV, respectively, as estimated from the corresponding derivative plots (Fig. 8). The band gap values clearly indicate that a small amount doping of Ni in $LiNi_xMn_{2-x}O_{4-\delta}S_\delta$ (where, $x = 0.2–0.3$ and $\delta \leq 0.1$) has little influence on the band gap, but an increased amount of Ni content in oxysulfide lowers the band gap, the minimum value observed is 1.35 eV for LMN4S ($LiNi_{0.4}Mn_{1.6}O_{4-\delta}S_\delta$.). The sample with highest Ni content i.e., $LiNi_{0.5}Mn_{1.5}O_{4-\delta}S_\delta$ shows a band gap of 1.39 eV. This may be due to the presence of trace amounts of impurity phases that may reduce the interaction between Ni 3d and O 2p orbitals. Such singular behaviour with respect to the band gap value and the absorption profile for LMN5S agree well with the results obtained from FTIR and microstructure analyses. In a similar way, the room-temperature electrical conductivity of LMN2S is found to be $\sim 10^{-5}$ S cm^{-1} and does not change significantly for Ni contents ≤ 0.4. For LMN5S, however, the electrical conductivity decreases by an order of magnitude.

The initial charge–discharge curves of $Li/LiNi_xMn_{2-x}O_{4-\delta}S_\delta$ coin cells over a voltage range of 5.0–3.4 V are given in Fig. 9. A flat plateau in both the 4 and 5 V regions is observed and originate from the oxidation of Mn^{3+}/Mn^{4+} and Ni^{3+}/Ni^{4+}, respectively. A sum-

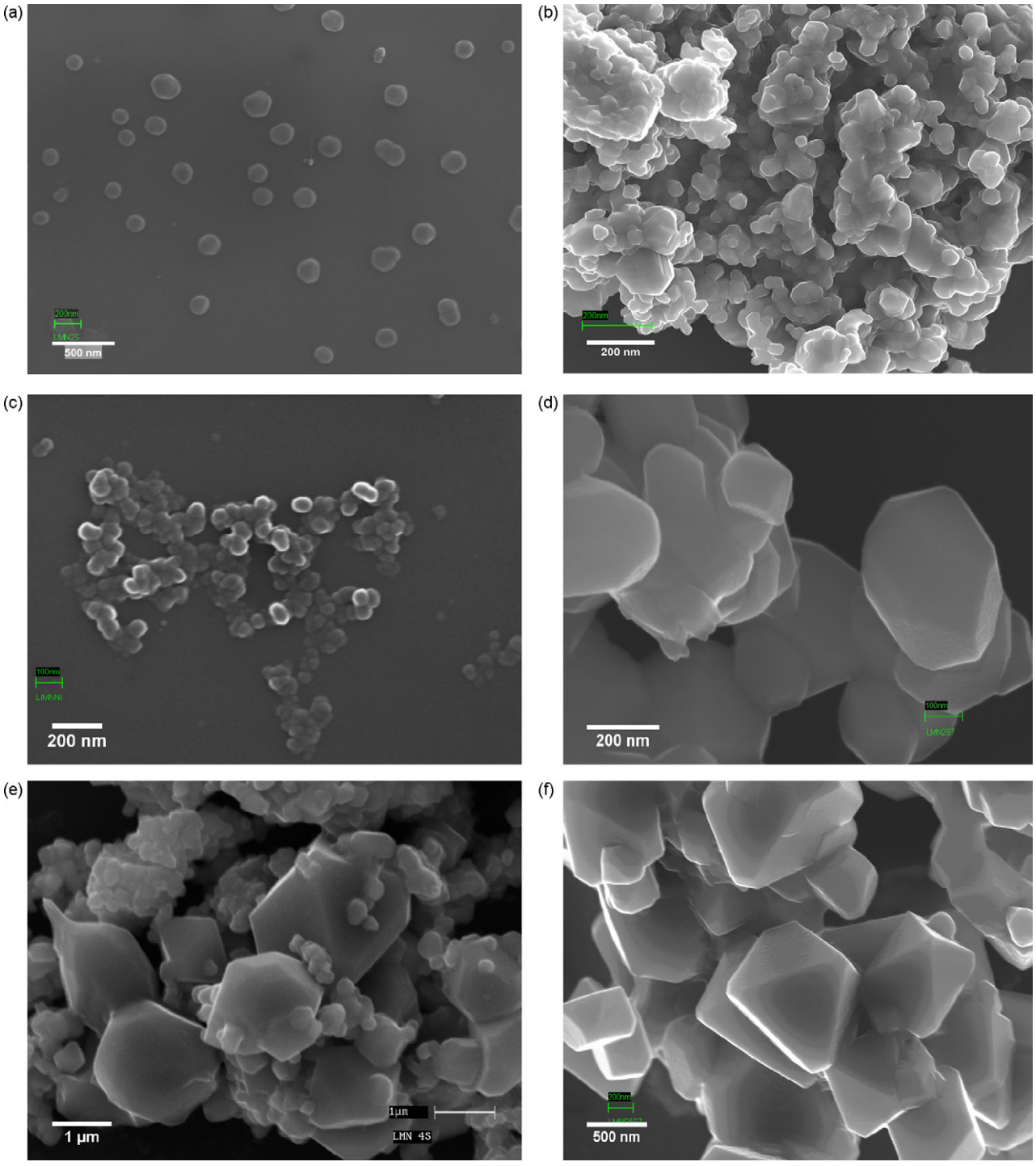

Fig. 5. FESEM micrographs of (a) LMN2S as-synthesized powder showing agglomeration free morphology, (b) LM, (c) LMN5, (d) LMN2S, (e) LMN4S, and (f) LMN5S [(b)–(f) are calcined powder fired at 700 °C].

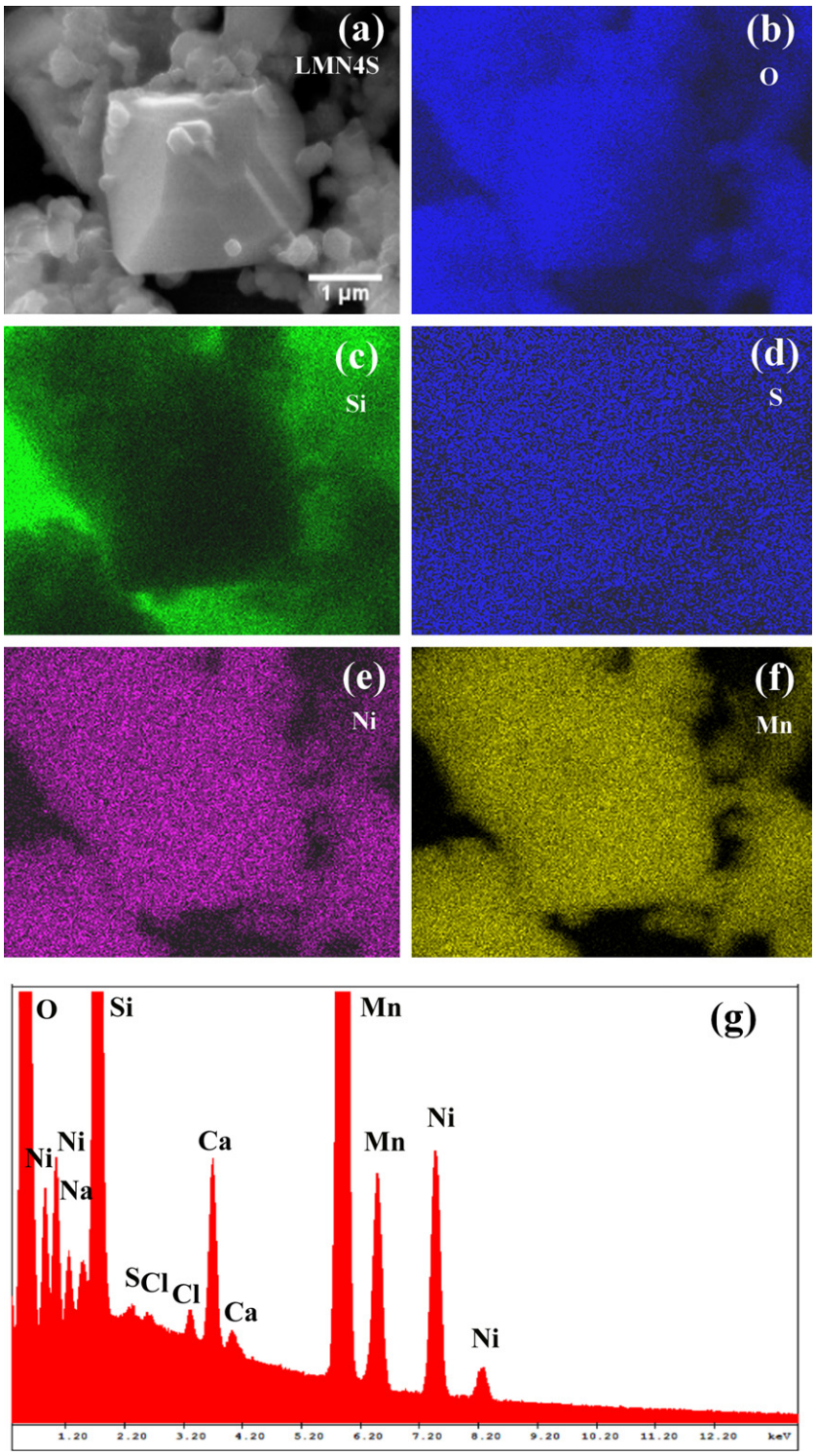

Fig. 6. (a) FESEM image of a selected area of LMN4S, (b)–(f) elemental mappings, and (g) EDX profile obtained from same area.

mary of the electrochemical results for different samples is given in Table 2. The total discharge capacity is divided into two parts: the capacity obtained in the 4 V region and the capacity obtained in the 5 V region. With increase in Ni content, the initial discharge capacity increases from 122 to 155 mAh g^{-1} when $x = 0.2$–0.4. A capacity of 120 mAh g^{-1} is observed for LMN2S and is comprised of a large 4 V capacity (75 mAh g^{-1}) and a small 5 V capacity (45 mAh g^{-1}). For LMN3S, the 4 V capacity is drastically reduced to 14 mAh g^{-1} while the 5 V capacity significantly increases to 108 mAh g^{-1}. With further increase in Ni content, for LMN4S, the 4 V capacity is regained to 55 mAh g^{-1}, whereas the 5 V capacity is reduced and just marginally results in a very high total capacity of 155 mAh g^{-1}. For LMN5S, the sample with the highest Ni content, the 4 V capacity increases to 67 mAh g^{-1}, but the 5 V capacity is drastically reduced to only 43 mAh g^{-1}. These values are similar to those for LMN2S. In fact, the initial charge discharge profiles for LMN2S and LMN5S are very similar (Fig. 9). This may be due to the fact that for LMN5S, the formation of Mn^{3+} ions cannot be avoided completely during cal-

Table 2
Electrochemical performance of various Ni-doped oxysulfide systems.

Sample	Discharge capacity at initial charge–discharge cycle ($mAh\,g^{-1}$)			Discharge capacity ($mAh^2\,g^{-1}$) of first cycle at a current density of 0.2 $mA\,cm^{-2}$	Discharge capacity of 25th cycle at a current density of 0.2 $mA\,cm^{-2}$ ($mAh\,g^{-1}$)			Capacity retention w.r.t. to first cycle	Capacity fading rate at 0.2 $mA\,cm^{-2}$, $F = C_{nth} - C_{1st}$ ($mAh\,g^{-1}\,cycle^{-1}$)
	4 V (3.4–4.5)	5 V (4.5–5)	Total capacity		4 V (3.4–4.5)	5 V (4.5–5)	Total capacity		
LMN2S	75	45	120	107	74	32	106	88%	0.04
LMN3S	14	108	122	109	24	76	100	82%	0.36
LMN4S	55	100	155	126	54	81	135	87%	No fading
LMN5S	67	43	120	105	58	32	90	75%	0.2

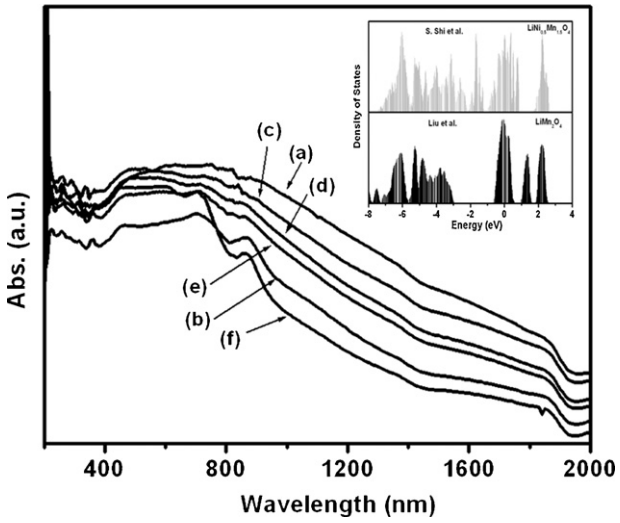

Fig. 7. UV–vis absorption spectra taken in reflectance mode of the samples (a) LM, (b) LMN5, (c) LMN2S, (d) LMN3S, (e) LMN4S, and (f) LMN5S. Inset shows total theoretical density of states of $LiMn_2O_4$ and $LiNi_{0.5}Mn_{1.5}O_4$ (Liu et al. and Shi et al. [38,39]).

cination in air. Again, stoichiometric loss of Ni from the LMN5S spinel matrix and formation of NiO may be responsible for the presence of Mn^{3+} ions and the reduction in the 5 V capacity. That the resulting Ni-deficiency in the spinel phase involves the presence of significant amounts of Mn^{3+} is evidenced by the occurrence of a 4 V plateau in LMN5S. These results are in good agreement with those of UV–vis spectroscopy, where the LM4S sample has shown the lowest band gap value that might have facilitated the charge transfer process. Wu et al. [40] have reported a value of 127 $mAh\,g^{-1}$ for a $LiNi_{0.5}Mn_{1.5}O_4$ sample synthesized by the sol–gel method, whereas Sun and co-workers [41] have obtained an initial capacity value of 138 $mAh\,g^{-1}$ for the same compound synthesized by the spray-pyrolysis method. Therefore, co-doping of pristine $LiMn_2O_4$ with Ni and S in this investigation results in the highest initial capacity value of 155 $mAh\,g^{-1}$ for $LiNi_{0.4}Mn_{1.6}O_{4-\delta}S_{\delta}$.

Fig. 10 presents capacity vs. cycle number plots for LM, LMN2S, LMN3S, LMN4S and LMN5S cells at a current density of 0.2 $mA\,cm^{-2}$ in a potential window of 3.4–5.0 V. The results are summarized in Table 2. The pristine $LiMn_2O_4$/Li cell shows a drastic fall in capacity and gives a value of 46 $mAh\,g^{-1}$ after 25 cycles, which is only 48% of its initial capacity (Fig. 10(a)). Such fast capacity fading is very common for pristine $LiMn_2O_4$ [42–44]. On the other hand, the LMN2S/Li cell delivers a capacity value of 106 $mAh\,g^{-1}$ after 25 cycles at the same current density (0.2 $mA\,cm^{-2}$), i.e., almost 88% capacity is retained with respect to the initial discharge capacity.

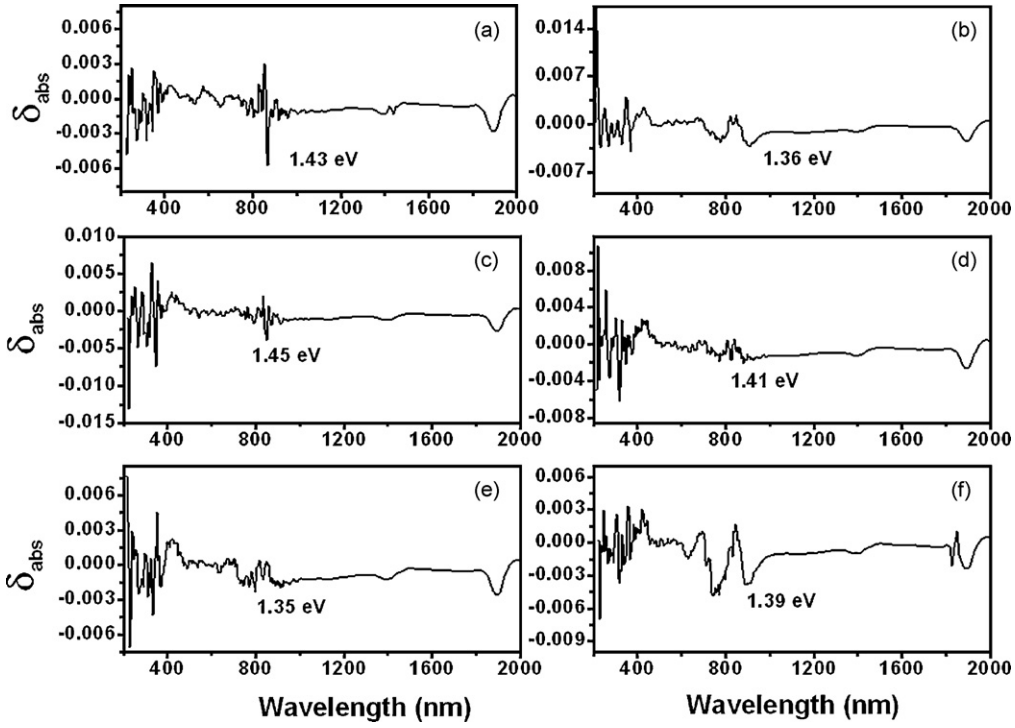

Fig. 8. Derivative of UV–vis absorption spectra of (a) LM, (b) LMN5, (c) LMN2S, (d) LMN3S, (e) LMN4S, and (f) LMN5S.

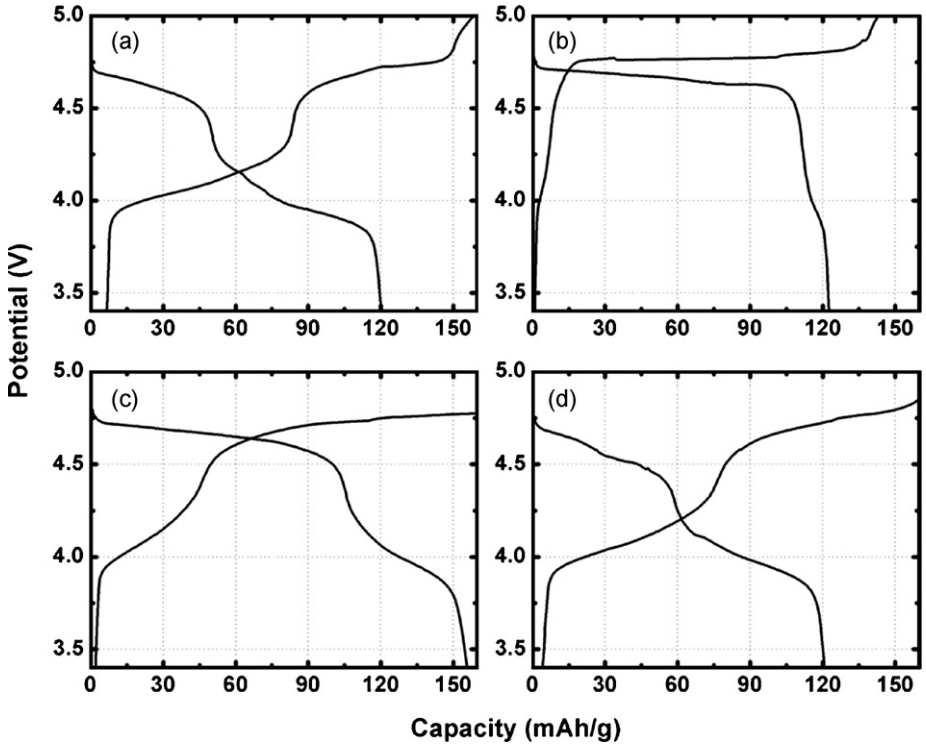

Fig. 9. Initial charge–discharge profiles of (a) LMN2S, (b) LMN3S, (c) LMN4S, and (d) LMN5S coin cells vs. Li.

Likewise for LMN3S and LMN4S, 82% and 87% capacity is retained after 25 cycles. The first cycle discharge capacity at a current density of 0.2 mA cm^{-2} for the LMN4S/Li cell is 126 mAh g^{-1}, but its capacity gradually increases during cycling and reaches to a value of 135 mAh g^{-1}, i.e., no capacity fading per cycle is observed for the LMN4S/Li cell at this current density. The performance may be due to the fact that the catalytic activity of sulfur is much more prominent in the LMN4S sample which may reinforce the spinel structure and restrict its structural degradation when cycling at voltages above 4.5 V. In general, however, the capacity fading rate

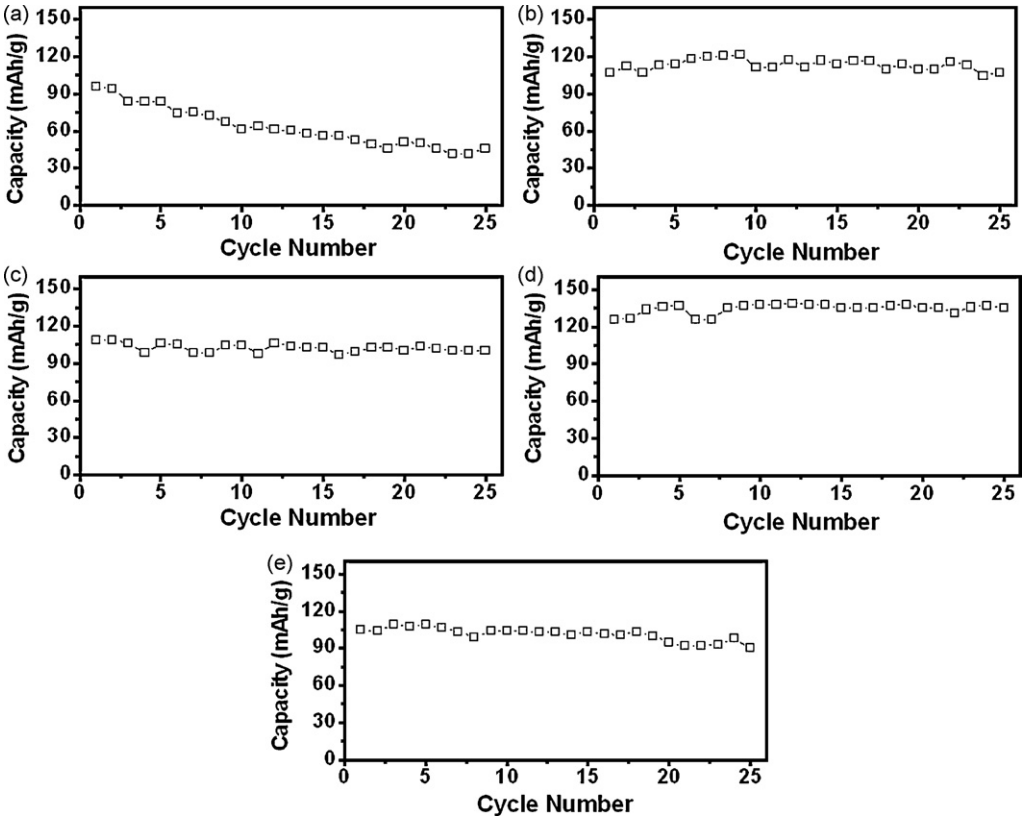

Fig. 10. Capacity vs. cycle number plots for (a) LM, (b) LMN2S, (c) LMN3S, (d) LMN4S, and (e) LMN5S cell at a current density of 0.2 mA cm^{-2}.

(0.04–0.2 mAh g^{-1} per cycle) is very small in case of all the oxysulfide systems studied highlighting the remarkable effect induced by co-doping of Ni and S.

4. Conclusions

The effect of co-doping of Ni and S into $LiMn_2O_4$ has been investigated by preparing a series of Ni-doped lithium manganese oxysulfide compounds by a cost-effective, alanine-assisted combustion process. It is found that co-doping of Ni and S in the spinel matrix has a distinct effect on the microstructure, band gap and electrochemical performance. All four oxysulfide systems exhibit excellent cycleability with good capacity retention. Among them, $LiNi_{0.4}Mn_{1.6}O_{4-\delta}S_{\delta}$ is the best composition with respect to capacity and also cycleability. An initial discharge capacity of 155 mAh g^{-1} and a steady capacity of 135 mAh g^{-1} during cycling at 0.2 mA cm^{-2} with practically no fading up to 25 cycles highlight the remarkable effect of Ni doping in presence of S in $LiMn_2O_4$, and the possible use of this material as a 5 V cathode in lithium-ion batteries.

Acknowledgements

The authors wish to thank Director, CGCRI, Kolkata for permission to publish this work. M.W.R. also acknowledges CSIR for a Senior Research Fellowship. The authors are also grateful to thank Ashok K. Mondal, SEM-ESCA Section, CGCRI for EDX measurements.

References

[1] T. Ohuzuku, M. Kitagawa, T. Hirai, J. Electrochem. Soc. 137 (1990) 760.
[2] W.J. Macklin, R.J. Neat, R.J. Powell, J. Power Sources 34 (1991) 39.
[3] V. Manev, A. Momchilov, A. Nassalevska, A. Kozawa, J. Power Sources 41 (1993) 305.
[4] D. Guyomard, J.M. Tarascon, Solid State Ionics 69 (1994) 222.
[5] J.M. Tarascon, W.R. Mckinnon, F. Coowar, T.N. Boowner, G. Amatucci, D. Guyomard, J. Electrochem. Soc. 141 (1997) 22.
[6] X. Wu, S.B. Kim, J. Power Sources 109 (2002) 53.
[7] G.T.-K. Fey, C.-Z. Lu, T.P. Kumar, J. Power Sources 115 (2003) 332.
[8] R. Alcántara, M. Jaraba, P. Lavela, J.L. Tirado, Chem. Mater. 15 (2003) 2376.
[9] L. Hernán, J. Morales, L. Sánchez, J. Santos, Solid State Ionics 118 (1999) 179.
[10] E. Iwata, K. Takahashi, K. Maeda, T. Mouri, J. Power Sources 81–82 (1999) 430.
[11] Y. Xia, T. Sakai, T. Fujieda, X.Q. Yang, X. Sun, Z.F. Ma, J. McBreen, M. Yoshio, J. Electrochem. Soc. 148 (2001) A72.
[12] G. Pistoia, G. Wang, Solid State Ionics 66 (1993) 135.
[13] D. Song, H. Ikuta, T. Uchida, M. Wakihara, Solid State Ionics 117 (1999) 151.
[14] R.J. Gummow, A. Kock, M.M. Thackeray, Solid State Ionics 69 (1994) 59.
[15] J.M. Amarilla, J.L.M. Vidales, R.M. Rojas, Solid State Ionics 127 (2000) 73.
[16] X.X. Xu, J. Yang, Y.Q. wang, J. Power Sources 174 (2007) 1113.
[17] M. Molenda, R. Dziembaj, E. Podstawka, W. Łasocha, L.M. Proniewicz, J. Phys. Chem. Solids 67 (2006) 1347.
[18] J.H. Lee, J.K. Hong, D.H. Jang, Y.K. Sun, S.M. Oh, J. Power Sources 89 (2000) 7.
[19] G.G. Amatucci, US Patent No. 5,759,720 (1998).
[20] S.H. Park, K.S. Park, Y.K. Sun, K.S. Nahm, J. Electrochem. Soc. 147 (2000) 2116.
[21] P. Barboux, J.M. Tarascon, F.K. Shokoohi, J. Solid State Chem. 94 (1991) 185.
[22] J.M. Tarascon, E. Wang, F.K. Shokoohi, W.R. McKinnon, S. Colson, J. Electrochem. Soc. 138 (1991) 2859.
[23] H. Huang, P.G. Bruce, J. Power Sources 54 (1995) 52.
[24] Q. Zhong, A. Banakdarpour, M. Zhang, Y. Gao, J.R. Dahn, J. Electrochem. Soc. 144 (1997) 205.
[25] T.A. Arunkumar, A. Manthiram, Electrochim. Acta 50 (2005) 5568.
[26] D.S. Ahn, M.Y. Song, J. Electrochem. Soc. 147 (2000) 874.
[27] Q. Zhong, A. Bonakdarpour, M. Zhang, Y. Gao, J.R. Dahn, J. Electrochem. Soc. 144 (1997) 205.
[28] S.H. Park, K.S. Park, S.S. Moon, Y.K. Sun, K.S. Nahm, J. Power Sources 92 (2001) 244.
[29] Y.J. Wei, L.Y. Yan, C.Z. Wang, X.G. Xu, F. Wu, G. Chen, J. Phys. Chem. B 108 (2004) 18547.
[30] M.W. Raja, S. Mahanty, P. Ghosh, R.N. Basu, H.S. Maiti, Mater. Res. Bull. 42 (2007) 1499.
[31] J.H. Kim, S.T. Myung, C.S. Yoon, S.G. Kang, Y.K. Sun, Chem. Mater. 16 (2004) 906.
[32] H. Fang, Z. Wang, B. Zhang, X. Li, G. Li, Electrochem. Commun. 9 (2007) 1077.
[33] Y.K. Sun, Electrochem. Commun. 2 (2000) 6.
[34] D. Fatcasiu, J.Q. Li, S. Cameron, Appl. Catal. 154 (1997) 173.
[35] T.W. Zawidzki, P.S. Apte, M.R. Hoare, J. Am. Ceram. Soc. 67 (1984) 361.
[36] J.B. Goodenough, Solid State Ionics 69 (1994) 184.
[37] M.W. Raja, S. Mahanty, M. Kundu, R.N. Basu, J. Alloys Compd. 468 (2008) 258.
[38] Y. Liu, T. Fuziwara, M. Morinaga, Solid State Ionics 126 (1999) 459.
[39] S. Shi, C. Ouyang, D.-S. Wang, L. Chen, X. Huang, Solid State Commun. 126 (2003) 531.
[40] H.M. Wu, J.P. Tu, X.T. Chen, D.Q. Shi, X.B. Zhao, G.S. Cao, Electrochim. Acta 51 (2006) 4148.
[41] H. Park, S.-W. Oh, S.T. Myung, Y.C. Kang, Y.K. Sun, Solid State Ionics 176 (2005) 481.
[42] W. Xiaomei, Z. Xiangfu, Y. Qinghe, J. Zhongkao, W. Haoqing, J. Fluorine Chem. 107 (2001) 39.
[43] T. Yi, X. Hu, K. Gao, J. Power Sources 162 (2006) 636.
[44] H.J. Bang, V.S. Donepudi, J. Prakash, Electrochim. Acta 48 (2002) 443.